Phase Transformations in Metals during Additive Manufacturing Processes

Jiawen Xie

Dept. of Aerospace Engineering, University of Michigan, Ann Arbor, MI 48109
Dassault Systèmes SIMULIA Corp., Johnston, RI 02919

Victor Oancea, Juan A. Hurtado
Dassault Systèmes SIMULIA Corp., Johnston, RI 02919

Abstract

The impetus of additive manufacturing (AM) technology in the last few years is significant. However, in many cases the reliability of the technology leads to parts that suffer from manufacturing defects and hence subpar strength and fatigue life when compared to parts manufactured with conventional technologies. Sustained experimentation is often required and computer simulations, like in many other fields before, are sought to provide significant insight into the process such that progress in raising the quality of AM parts can be achieved. This paper presents a sequential thermals-stress modelling approach of additive manufacturing processes of titanium alloy Ti-6Al-4V parts leveraging a new physics-based framework in a general-purpose finite element code (Abaqus). The framework allows for arbitrary meshes of CAD representations, accounts for the exact specification in time and space of machine tooling (e.g., powder addition, laser trajectories, dwell times, etc.) as would be used on an actual machine, precise integration of the moving energy sources (e.g., laser, electron beams), and automatic mesh independent computation of the continuously evolving convection and radiation surfaces. The constitutive models consider material-state transitions, solid-phase transformations and metal grain evolutions. In the heat transfer analysis, temperature-dependent thermal properties are considered, as well as latent heat effects of fusion and vaporization. The state of matter (powder, liquid, solid, metallurgical phases) was updated at every increment of the simulation based on the computed temperature histories by leveraging solid-phase transformation kinetics models. The grain size and morphology of the β-phase were also estimated automatically using published models and experimental measurements. Computed temperature distributions (space and time), material states, solid-phase composition, and grain structure serve as input into the mechanical stress analysis. Besides the usual thermal expansion and classical plasticity models, phase transformation induced volume change and plasticity are also considered. Temperature histories and distortions of printed parts of finite element (FE) simulations were validated with published measurements from a Laser Direct Energy Deposition (LDED) experiment.

1. Introduction

In metal-based additive manufacturing, represented by powder-bed fusion (PBF) and directed energy deposition (DED), metallic powder is deposited and locally melted by

an intense moving heat source (laser, electron beam, etc.). Upon cooling, the molten material solidifies and fuses to previously solidified underlying layers or to a substrate. Local temperature transients and thermal gradients in a workpiece during this layer-by-layer constructing process are strongly influenced by process parameters, including but not limited to nominal power and heat distribution intensity, pattern and speed of scanning, cooling time between beads and layers, thickness and of the powder layer, and ambient temperature conditions. The thermal histories can be essential to the resultingmicrostructure composition, evolution of grain size and morphology, defects, residual stress and distortion, which can further influence the performance of the final product in terms of stiffness, strength and life (Shamsaei *et al.*, 2015). A comprehensive understanding of the influence of those process parameters on the mechanical performance of the products is important. Though real physical experiments are valuable and necessary for validation and calibration purposes, virtual manufacturing based on computer aided modeling and simulations can provide an efficient way to explore more possibilities of process optimization with lower costs and faster turnaround times.

The efforts to develop numerical techniques to simulate certain aspects of an additive manufacturing process are numerous and span several communities of scientists and engineers from academics to applied research commercial entities. The difficulties to capture/predict via computer simulations such processes are many, including:

- Vastly different time scales of the melting/solidification physics (miliseconds) and the overall manufacturing time of a typical part (hours of printing on the machine).

- Wide range of scale lengths from microns associated with melt pools to hundreds of millimetres (or more) necessary to model a typical part.

- Rapidly evolving high temperature gradients around the "action" zone which leads to highly anisotropic material properties at the end of print (before eventual heat treatment).

Assuming that adequate models are employed, very large simulation times are typically necessary to model such processes in order to capture all of the above.

In this paper, a newly introduced physics-based framework in a general-purpose finite element code (Abaqus User's Manual, 2017) is leveraged as discussed briefly in the next section. The focus of this paper as described in subsequent sections is however on thermal and mechanical analysis of additive manufacturing processes of Ti-6Al-4V. In the transient heat transfer analysis, thermal properties are considered as depending on temperature while accounting for phase transformations based on phenomenological models. Temperature-induced solid-phase transformations, including martensitic and diffusional transformations, are modelled using Johnson-Mehl-Avrami (JMA) and Koistinen-Marburger (KM) models, respectively (Crespo, 2011). Thus, the solid-phase composition can be assessed at any location and time during the printing process. A differential form of a parabolic grain-growth law is used to estimate the size of β grains

during the solidification process (Kobryn and Semiatin, 2003). The β grain morphology, being equiaxed, columnar or a mixture of both, is estimated using an experimentally calibrated solidification map (Gockel and Beuth, 2013). The computed histories of temperature distributions, material states, microstructural characteristics further serve as input to a macroscopic mechanical model (Manhken *et al.*, 2009; Denlinger *et al.*, 2015a). Within the framework of classical thermo-elasto-plasticity theory, effects of transformation induced expansion and plasticity are also considered. An experiment conducted by (Denlinger *et al.*, 2015a) is taken to validate the virtual manufacturing based on finite element (FE) simulations.

2. Physics-based Computational Framework

The finite element method continues to be at the core of many CAE solutions. For that matter, it is no surprise that a variety of researchers as well as commercial CAE vendors have turned to FEM to address the challenging physics problems associated with Additive Manufacturing Process Simulation solutions. As implemented in Abaqus 2017 (Abaqus User's Manual, 2017), key features of the framework include:

A. Meshing: The geometric shape of the part whose 3D printing process is to be modelled is first discretized with finite elements. Arbitrary meshes of arbitrary mesh densities can be used using existing pre-processors. Using such meshes greatly improves on streamlining the analysis process as typically AM fabricated parts have very complex shapes for which uniform or layer-conforming meshes are not really possible.

B. Machine information: The 3D printing machine related information (e.g., powder recoating sequence, laser scan path, material deposition of the printing head, etc.) is pre-processed with no loss of accuracy from actual data as used by the physical machines. As far as the modelling process is concerned, no loss of accuracy is thus encountered by simplifying the information that the printing machine would actually use.

C. A new "Intersection Module" is used to "intersect" the finite element mesh with the tool path information in a geometric sense. The intersection can be based on either the original shape of the part or the current shape of the predicted deformed/distorted shape of the part during the analysis.

D. Progressive element activation: At any given point during the simulation any particular finite element would be either completely filled with mater, partially filled with matter, or completely empty. The software keeps track of this evolution in a precise fashion.

E. Progressive heating computations: at any point in time, particular heat bursts are computed by taking into account the actual path (and power distribution) of the heat source. An arbitrary number of heating events (characterized as a sequence of heat fluxes at given locations) are computed for an accurate representation of the heating source in both time and space.

F. Progressive cooling via convection and radiation: partial facet areas are computed to allow for a very precise assessment of cooling related heat fluxes on any given finite element discretizations. Radiation and convection cooling can be modelled on a continuously evolving surface that reflects the actual tooling on the machine.

3. Thermal Analysis

The basic energy balance of uncoupled heat transfer analysis is

$$\int_V \rho \dot{U} \delta T \, dV - \int_V \boldsymbol{f} \cdot \delta \boldsymbol{g} \, dV = \int_V r \delta T \, dV + \int_S q \delta T \, dS \tag{1}$$

where V is a volume of material, with surface area S; ρ is the density of the material; $\dot{U} = \frac{dU}{dt}$ is the material time rate of the internal energy; T is the temperature; q is the heat flux per unit area of the body, flowing into the body; and r is the heat supplied internally into the body per unit volume. Fourier's law states that

$$\boldsymbol{f} = -k \cdot \boldsymbol{g} \tag{2}$$

where $\boldsymbol{f}$ is the heat flux, k is the thermal conductivity and $\boldsymbol{g} = \nabla T$ is the temperature gradient.

Latent heat effects at transitions between states of matters, such as melting from solid state to liquid state, are modelled using an additional term in the internal thermal energy and assumed to vary linearly with temperature. Thus, the change of internal energy can be written as

$$dU = c_p dT + dU_{latn} \tag{3}$$

where c_p is the specific heat capacity, dT is the change of temperature, and dU_{latn} is the change of latent heat between transition between solidus and liquidus. Denoting starting temperature T_1 and ending temperature T_2,

$$dU_{latn} = \begin{cases} 0 & T \leq T_1 \ or \ T \geq T_2 \\ \dfrac{U_{latn}}{T_2 - T_1} dT & T_1 < T < T_2 \end{cases} \tag{4}$$

In this study, the laser heat source is considered as a distributed volumetric heat flux and modelled by Goldak's semi-ellipsoid model (Goldak, 1984). In the local *x-y-z* frame of the laser, where *x*-axis aligns with the laser moving direction, the laser heat source is described as

$$Q(x, y, z, t) = \frac{2P\eta}{\bar{a}\bar{b}\bar{c}\pi\sqrt{\pi}} \exp\left[-\left(\frac{(x + v_x t)^2}{\bar{a}^2} + \frac{(y)^2}{\bar{b}^2} + \frac{(z)^2}{\bar{c}^2}\right)\right] \tag{5}$$

where P is the nominal power, η is absorption coefficient and v_x is the moving speed of the laser; t is the time; $\bar{a}$, $\bar{b}$, and $\bar{c}$ are the dimensions of the ellipsoid along x-, y- and z-axis, respectively. The dimensions can be defined by laser parameters, including radius r, eccentricity e and penetration depth d, as

$$\bar{a} = er, \;\; \bar{b} = \frac{r}{e}, \;\; \bar{c} = d \tag{6}$$

Thermal radiation

$$q_{rad} = \varepsilon\sigma((T - T_z)^4 - (T_\infty - T_z)^4) \tag{7}$$

and surface convection

$$q_{conv} = h(T - T_\infty) \tag{8}$$

of free surfaces during manufacturing processes are considered, where ε is the material emissivity, h is convective coefficient, $\sigma = 5.67 \times 10^{-8}$ W/(m$^2 \cdot$ °C^4) is the Stefan-Boltzmann constant, $T_z = -273.15$ °C is the absolute zero temperature, and T_∞ is the ambient temperature.

During additive manufacturing processes, at least three material states can coexist in one workpiece. Metallic powder, or more generally, raw materials, are melted to liquid state by the laser. The liquid undergoes cooling and solidification when the laser is removed. The solidified material can be re-melted when the laser passes by a nearby location or is applied on the upper layers of raw material. It has been found that thermal conductivity and specific heat capacity of metallic powder can be significantly different from those of solid bulk material (Shen and Chou, 2012). Therefore, it is important to identify different material states in the thermal analysis. Transitions between those three material states are considered as simply governed by temperature. As shown in Figure 1, all transitions occur in a temperature range bonded by the solidus and liquidus temperatures of the alloy. Within the temperature range, the material is considered as the mixture of two transforming states. It should be noticed that the transition from raw material to liquid state is non-reversible while the transitions between solid state and liquid state is reversible.
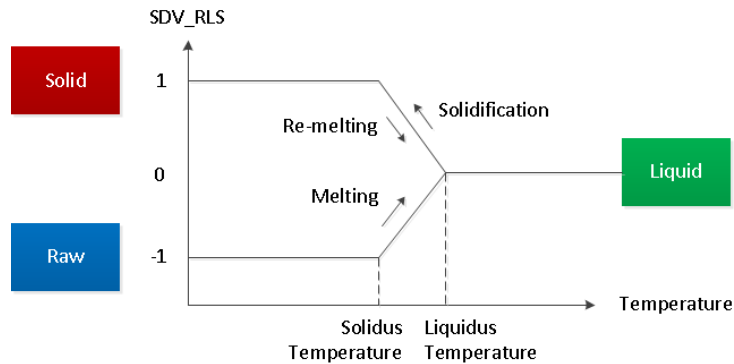
Table 1 shows the temperature-dependent thermal conductivity and specific heat capacity of Ti-6Al-4V (Fan and Liou, 2012) used in this study. These values are used for both solid and liquid states. The values for the raw material (e.g. powder form) are assumed to be a fraction of those of the solid state at 10 °C. The latent heat of fusion and vaporization is also considered, as summarized in Table 2 (Fan and Liou, 2012). Both latent heat effects are reversible. The density, the emissivity and the convection coefficient are assumed constant (Denlinger and Michaleris, 2016), shown in Table 3.

Temperature [°C]	Conductivity k[W/(m · °C)]	Specific Heat Capacity c_p[J/(kg · °C)]
Solid and Liquid States		
10	5.705	543.9
110	7.275	565.4
210	8.845	586.9
310	10.415	608.4
410	11.985	629.9
510	13.555	651.4
610	15.125	672.9
710	16.695	694.4
810	18.265	715.9
910	19.835	737.4
1010	21.45	758.9
1110	22.975	780.4
1210	24.545	801.9
1310	23.619	697.8
1410	24.889	715.8
1510	26.159	733.8
1610	27.429	751.9

Table 1:   **Thermal conductivity and specific heat capacity of Ti-6Al-4V.**

Latent heat of fusion	2.86×10^5 J/kg
Solidus temperature	1604 °C

Liquidus temperature	1650 °C
Latent heat of vaporization	9.83×10^6 J/kg
Liquidus temperature	3290 °C
Vaporized temperature	3390 °C

Table 2: Latent heat of Ti-6Al-4V.

Density ρ	4420 kg/m^3
Emissivity ϵ	0.25
Convection Coefficient h	18 W/(m$^2 \cdot$ °C)

Table 3: Other thermal properties of Ti-6Al-4V.

4. Solid-phase Transformations

The microstructure of rapid manufactured Ti-6Al-4V products consists primarily of a hexagonal close-packed (hcp) α-phase, a body-centred cubic (bcc) β-phase, and a martensitic α'-phase. The material is considered to fully consist of β-phase right after solidification. Different temperature-induced transformations can occur later between those three solid phases as the material undergoes cooling and subsequent heating/cooling cycles. These transformations can be categorized as a martensitic transformation and two diffusional transformations that can be modelled using the Koistinen-Marburger (KM) and the Johnson-Mehl-Avrami (JMA) models, respectively (Crespo, 2011).

A martensitic transformation from β-phase to α'-phase, denoted as $\beta \rightarrow \alpha'$, can occur when the cooling rate is higher than $\dot{T}_{MT} = 410$ °C/s. The transformation solely depends on temperature, as described by the KM model,

$$f_{\alpha'}(T) = f_{\alpha'}(T_o) + \left(f_\beta(T_o) - f_{\beta_r}\right)[1 - \exp[-\gamma(M_s - T)]] \tag{9}$$

where $f_{\alpha'}$ and f_β are volume fractions of α'- and β-phase, respectively, T_o is the temperature at the beginning of the transformation, and $\gamma = 0.015$ °C^{-1}. The transformation occurs if the solid cools below the martensitic start temperature ($M_s = 650$ °C). An additional requirement is that the initial volume fraction of β-phase is higher than the retained amount of β-phase, namely, $f_\beta(T_o) > f_{\beta_r}$. Past studies have observed that a certain amount of β-phase can be retained because of the stabilized effect of vanadium (Crespo, 2011). A relation between the retained amount and the initial amount of β-phase is given as,

$$f_{\beta_r} = \begin{cases} f_\beta(T_o) & , f_\beta(T_o) < 0.25 \\ 0.25(1 - f_\beta(T_o)) & , f_\beta(T_o) \geq 0.25 \end{cases} \tag{10}$$

Under arbitrary thermal histories the volume fraction of α'-phase is updated using a backward Euler integration of the differential form of the original KM model,

$$f_{\alpha'}(T + dT) = \frac{f_{\alpha'}(T) - \gamma dT\left(f_{\beta}(T_o) - f_{\beta_r} + f_{\alpha'}(T_o)\right)}{1 - \gamma dT} \tag{11}$$

Two diffusion controlled transformations can be observed: decomposition of martensitic α'-phase into a mixture of α- and β-phases, denoted as $\alpha' \rightarrow \alpha + \beta$, which only occurs during heating; transformations between α- and β-phases, denoted as $\beta \leftrightarrow \alpha$, which can occur during heating or slow cooling.

The kinetics of those diffusional transformations under isothermal conditions can be described by a series of JMA equations,

$$\alpha' \rightarrow \alpha + \beta: \quad f_{\alpha'} = 1 - (1 - \exp[-k_2 t^{n_2}])(1 - f_{\alpha'}^{eq}), \qquad \text{if } f_{\alpha'} > f_{\alpha'}^{eq}$$

$$\beta \rightarrow \alpha: \qquad f_{\beta} = 1 - f_{\alpha'} - (1 - \exp[-k_3 t^{n_3}])\left(1 - f_{\alpha'} - f_{\beta}^{eq}\right), \text{if } f_{\beta} > f_{\beta}^{eq} \tag{12}$$

$$\alpha \rightarrow \beta: \qquad f_{\beta} = (1 - \exp[-k_3 t^{n_3}])f_{\beta}^{eq}, \qquad\qquad \text{if } f_{\beta} < f_{\beta}^{eq}$$

where $f_{\alpha'}^{eq}$ and f_{β}^{eq} are temperature-dependent equilibrium volume fractions of α'- and β-phase, respectively. Additionally,

$$f_{\beta}^{eq} = f_{\beta,0}^{eq}(1 - f_{\alpha'}) \tag{13}$$

where $f_{\beta,0}^{eq}$ is the equilibrium volume fraction of β-phases in the mixture that only contains α- and β-phases. The equilibrium volume fractions have been experimentally determined (Marion *et al.*, 2014; Castro and Seraphin, 1966),

$$f_{\alpha'}^{eq}(T) = \frac{1}{2}\left(1 + \tanh\left(\frac{c_1 - T}{c_2}\right)\right) \tag{14}$$

$$f_{\alpha,0}^{eq}(T) = \begin{cases} c_3\left(1 - e^{-c_4(T_{\beta-transus} - T)}\right) & ,T \leq T_{\beta-transus} \\ 0 & ,T > T_{\beta-transus} \end{cases} \tag{15}$$

$$f_{\beta,0}^{eq}(T) = 1 - f_{\alpha,0}^{eq}(T) \tag{16}$$

where constants are $c_1 = 450\ °C$, $c_2 = 80\ °C$, $c_3 = 0.925$, $c_4 = 0.0085\ °C^{-1}$, and $T_{\beta-transus} = 980\ °C$ is the lowest temperature at which the microstructure fully consists of β-phase. The transformation coefficients, k_2, n_2, k_3, n_3, can also be measured experimentally from time temperature transformation (TTT) diagram (Mur *et al.*, 1996; Malinov *et al.,* 2001), as shown in Table 4.

Temperature [°C]	k_2 [s$^{-n_2}$]	n_2 [−]
400	0.0192	0.667
500	0.0147	1.106
700	0.0246	1.252
800	0.0307	1.326
Temperature [°C]	k_3 [s$^{-n_3}$]	n_3 [−]
750	0.028	1.04
800	0.026	1.34
850	0.022	1.38
870	0.025	1.34
900	0.046	1.21
925	0.024	1.39
950	0.017	1.41

Table 4:   Temperature-dependent diffusional transformation coefficients.

The original JMA model, which was proposed for isothermal conditions, has been extended to model non-isothermal conditions by considering continuous temperature variation as a series of small consecutive isothermal steps (Crespo, 2011). The kinetics of the transformation $\alpha' \rightarrow \alpha + \beta$ is given as

$$f_{\alpha'}(T + dT) = 1 - (1 - \exp[-k_2(\xi_{\alpha'} + \Delta t)^{n_2}])\left(1 - f_{\alpha'}^{eq}\right), \quad \text{if } f_{\alpha'} > f_{\alpha'}^{eq} \quad (17)$$

where $\xi_{\alpha'}$ is the fictitious time which would provide the same amount of transformation, resulted in volume fraction, $f_{\alpha'}(T)$, at a constant temperature $T + dT$. Thus, $\xi_{\alpha'}$ can be derived from the isothermal JMA equation,

$$\xi_{\alpha'} = \left[-\frac{1}{k_2} \ln\left(\frac{f_{\alpha'}(T) - f_{\alpha'}^{eq}}{1 - f_{\alpha'}^{eq}} \right) \right]^{\frac{1}{n_2}} \quad (18)$$

The transformation also results in changes of volume fractions of α- and β-phases, which are assumed as proportional to their volume fractions at temperature T. Thus, the intermediate volume fractions of α- and β-phases are,

$$f_\alpha^* = \frac{1 - f_{\alpha'}(T + dT)}{1 - f_{\alpha'}(T)} f_\alpha(T) \quad (19)$$

$$f_\beta^* = \frac{1 - f_{\alpha'}(T + dT)}{1 - f_{\alpha'}(T)} f_\beta(T) \quad (20)$$

The kinetics of transformations $\beta \leftrightarrow \alpha$ can be defined as

$$\beta \to \alpha: \quad f_\beta(T + dT) = 1 - f_{\alpha'} - \left(1 - \exp\left[-k_1(\xi_\beta + \Delta t)^{n_1}\right]\right)\left(1 - f_{\alpha'} - f_\beta^{eq}\right),$$

$$\text{if } f_\beta^* > f_\beta^{eq}(T + dT)$$

$$\alpha \to \beta: \quad f_\beta(T + dT) = \left(1 - \exp\left[-k_1(\xi_\beta + \Delta t)^{n_1}\right]\right)f_\beta^{eq}, \qquad \text{if } f_\beta^* < f_\beta^{eq}(T + dT)$$

$$\text{No transformation:} \quad f_\beta(T + dT) = f_\beta^*, \qquad\qquad\qquad \text{if } f_\beta^* = f_\beta^{eq}(T + dT)$$

$$(21)$$

The solid-phase transformations of Ti-6Al-4V are summarized in Table 5.

Transformation		Type	Occurring Conditions	
1	$\beta \to \alpha'$	Martensitic	$\dot{T} < -\dot{T}_{MT} = -410°C/s$ (rapid cooling) And $T \leq M_s$	And $f_\beta > f_{\beta_r}$
2	$\alpha' \to \alpha + \beta$	Diffusional	$\dot{T} > 0$ (heating)	And $f_{\alpha'} > f_{\alpha'}^{eq}$
3	$\beta \to \alpha$		$\dot{T} > -\dot{T}_{MT}$ (slow cooling or heating)	And $f_\beta^* > f_\beta^{eq}$
3R	$\alpha \to \beta$			And $f_\beta^* < f_\beta^{eq}$

Table 5:   **Summary of solid-phase transformations of Ti-6Al-4V.**

A simple test was performed to validate the model of material-state transitions and solid-phase transformations. A rapid heating-cooling cycle, followed by a slow heating-cooling cycle, with temperatures of both ranging from 26 °C to 1826 °C, was assigned to the analysis. As shown in Figure 2, melting and re-melting start when temperature is above the solidus temperature and complete when the temperature rises to the liquidus temperature. Similarly, the solidification occurs in the same range of temperature during cooling. As mention earlier, the microstructure is fully β-phase right after the solidification. The β-phase completely transforms to α'-phase during rapid cooling. The two diffusional transformations occur slowly during the subsequent slow heating-cooling cycle.
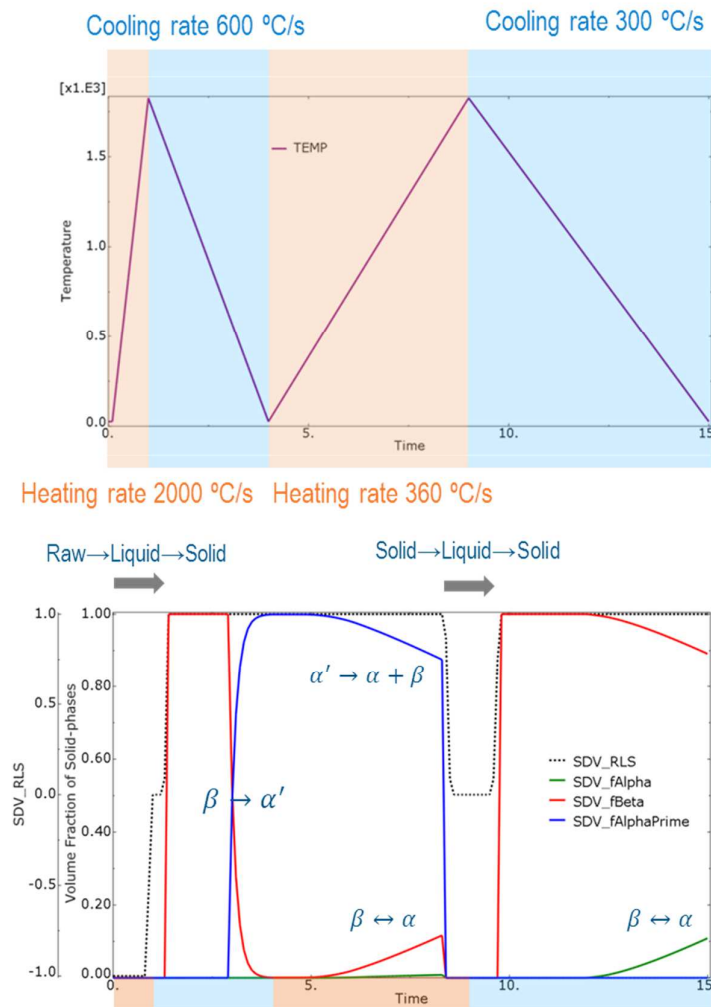
Figure 2:   Temperature assignment (top), and results of material-state transitions and solid-phase transformations (bottom) of the test.

5.   Grain Size and Morphology

Many mechanical properties are governed by grain size, microstructure morphology and composition of solid phases. While the α grain structure can be modified by post-process heat treatment, the β grain structure remains mostly unchanged (Gockel and Beuth, 2013). The β grain structure is known to play a significant effect on fatigue performance, therefore it is important to provide information of β grain size and morphology of the products based on the process histories

The β grain size is estimated by a parabolic growth law (Kobryn and Semiatin, 2003). Isothermally, one will have

$$d^n - d_0^n = k\,t\,\exp\left(-\frac{Q}{R(T - T_z)}\right) \tag{22}$$

where d is the grain size at time t; $d_0 = 0$ is the initial grain size, $n = 2$, $k = 2.2$ m^2/s are coefficients, and $Q = 251$ kJ/mol is an activation energy of β-phase of Ti-6Al-4V; $R = 8.314$ J/(mol · °C) is the universal gas constant. For non-isothermal conditions, the grain size is updated incrementally by numerical integration of the differential form of the parabolic growth law using the backward Euler method,

$$d_{t+\Delta t}^n = d_t^n + \Delta t\,k\,\exp\left(-\frac{Q}{R(T - T_z)}\right) \tag{23}$$

The growth of β grain size is assumed as occurring within a temperature range, bounded by the β-transus temperature and the solidus temperature.

The β grain morphology, being equiaxed, columnar or their mixture, can be predicted using an experimentally measured solidification map. Equiaxed grains have isotropic dimensions while columnar grains are elongated in one direction (Gockel and Beuth, 2013). The solidification map of Ti-6Al-4V with calibrated boundaries of fully equiaxed and fully columnar grains is shown in Figure 3 (Kobryn and Semiatin, 2003). For a given combination of magnitude of thermal gradient G and solidification rate $R = \left|\frac{\dot{T}}{G}\right|$, the β grain morplogy can be determined by comparing the process combination with the map. If the combination is mapped to a point A in the mixed region, as shown in Figure 4, the volume fraction of columnar grains can be evaluated as the ratio of the distance $\overline{AB}$ between the data point A and the columnar boundary line, and the distance $\overline{BC}$ between the two boundaries, both measured along the line of constant grain size.
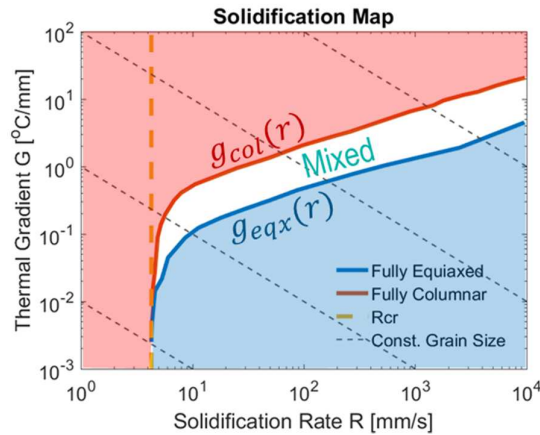

Figure 3: The solidification map of Ti-6Al-4V that is used to determine the β grain morphology.
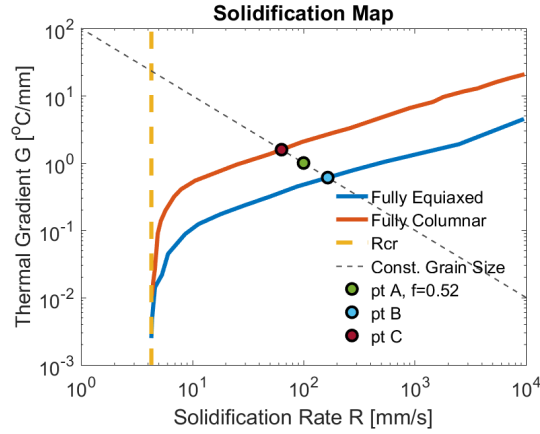
Figure 4:   *Determine the volume fractions of columnar grains $(\overline{AB}/\overline{BC})$ based on the solidification map.*

6.   Mechanical Modelling

Rapid temperature changes and high thermal gradients in workpieces during additive manufacturing processes can cause residual stresses. Distortions can also be observed in final products, and possibly caused by transitions of material states, formation of microstructures, porosity of powder layer, and plasticity. The mechanical performance of manufactured parts, including stiffness, strength and life, is directly related to the material microstructures (including grain size, morphology and porosity) and can be affected by the presence of residual stresses and distortions (Shamsaei *et al.*, 2015). Besides the semi-empirical laws mentioned in earlier sections, studies of microstructural evolutions during printing processes can also be found in micro scale simulations of dendritic morphology using cellular automata method (Yin and Felicelli, 2010) and phase field method (Sahoo and Chou, 2016). However, a comprehensive understanding of the relationship between microstructural characteristics and mechanical properties of additive manufactured parts is still a major challenge.

A phenomenological mechanical model has been suggested (Manhken *et al.*, 2009) as a simpler approach that only considers solid-phase transformations in metal forming processes. Within the framework of classical thermo-elasto-plasticity theory, transformation induced volumetric change and plasticity are also considered. The model, originally applied to a steel alloy with a single phase transformation, is extended to Ti-6AL-4V while also considering multiple solid-phase transformations.

The decomposition of total strain tensor is assumed as

$$\boldsymbol{\epsilon} = \boldsymbol{\epsilon}^{el} + \boldsymbol{\epsilon}^{\theta} + \boldsymbol{\epsilon}^{p} + \boldsymbol{\epsilon}^{tp} + \boldsymbol{\epsilon}^{tv} \qquad (24)$$

where $\boldsymbol{\epsilon}^{el}$ is the elastic strain tensor, $\boldsymbol{\epsilon}^{\theta}$ is the thermal expansion strain tensor, $\boldsymbol{\epsilon}^{p}$ is the plastic strain tensor, $\boldsymbol{\epsilon}^{tp}$ is the transformation induced plastic strain tensor, and $\boldsymbol{\epsilon}^{tv}$ is the transformation induced expansion strain tensor. The stress is given by

$$\boldsymbol{\sigma} = \boldsymbol{C}\boldsymbol{\epsilon}^{el} = \boldsymbol{C}\left(\boldsymbol{\epsilon} - \boldsymbol{\epsilon}^{\theta} - \boldsymbol{\epsilon}^{p} - \boldsymbol{\epsilon}^{tp} - \boldsymbol{\epsilon}^{tv}\right) \tag{25}$$

Here, $\boldsymbol{C}$ is the fourth-order elasticity tensor as a function of the elastic modules E and the Poisson's ratio v, which can depend on temperature and material states, and additionally, for the solid state, can be calculated from the solid-phase composition using a rule of mixture.

The rule of mixture of solid-phase composition is also applied to compute the thermal expansion strain tensor,

$$\Delta\boldsymbol{\epsilon}^{\theta} = \sum_{k=\alpha,\beta,\alpha'} \alpha_k^{\theta} f_k \Delta T \ \mathbf{I} \tag{26}$$

where α_k^{θ} is the coefficient of thermal expansion of each solid-phase. The classical formulation of isotropic plasticity is adopted, with yield stress given by the rule of mixture

$$\sigma_Y = \sum_{k=\alpha,\beta,\alpha'} \sigma_{Y(k)} f_k \tag{27}$$

The yield stress of individual solid-phases can be found in (Crespo *et al.*, 2009).

Similarly, the transformation induced plasticity and volumetric change can be evaluated by a rule of mixture of solid-phase transformations,

$$\Delta\boldsymbol{\epsilon}^{tp} = \sum_{k=1}^{3} \frac{3}{2} K_{tp}^k \boldsymbol{\sigma}^{dev} g'\left(f_{child}^k\right) \Delta f_{child}^k \tag{28}$$

$$\Delta\boldsymbol{\epsilon}^{tv} = \sum_{k=1}^{3} \frac{1}{3} K_{tv}^k \Delta f_{child}^k \ \mathbf{I} \tag{29}$$

where K_{tp}^k and K_{tv}^k are coefficients of plasticity and expansion induced by each transformation, respectively; $\boldsymbol{\sigma}^{dev}$ is the deviatoric part of the stress tensor; f_{child}^k is the volume fraction of the child phase of each transformation, *e.g.*, $f_{child}^k = f_{\alpha'}$ for the martensitic transformation. When the solid is melted to the liquid state, the transformation induced strains are reset to zero by letting

$$\Delta\boldsymbol{\epsilon}^{tp} = -\boldsymbol{\epsilon}^{tp} \tag{30}$$

$$\Delta\boldsymbol{\epsilon}^{tv} = -\boldsymbol{\epsilon}^{tv} \tag{31}$$

The numerical implementation of the model uses an implicit backward Euler integration scheme.

The transformation strains can be determined from transformation kinetics discussed previously. However, the coefficients K_{tp}^k and K_{tv}^k have not yet been measured or calibrated by experiments. A simplified version of the macroscopic mechanical model has been proposed by (Denlinger *et al.*, 2015a; Denlinger and Michaleris, 2016), assuming that stress relaxation occurs at a certain temperature as an effect of solid-phase transformations. Thus, the constitutive law and the strain decomposition follow the classical thermal-elasto-plasticity theory with the implicit backward Euler integration scheme,

$$\epsilon = \epsilon^{el} + \epsilon^{\theta} + \epsilon^{p} \tag{32}$$

$$^{n+1}\sigma = {}^{n}\sigma + \Delta\sigma \tag{33}$$

$$\Delta\sigma = C\left(\Delta\epsilon - \Delta\epsilon^{\theta} - \Delta\epsilon^{p}\right) + \Delta C\left({}^{n}\epsilon - {}^{n}\epsilon^{\theta} - {}^{n}\epsilon^{p}\right) \tag{34}$$

except that when the temperature is higher than the relaxation temperature, which is assumed as 690 °C for Ti-6Al-4V, stress and all strains of previous increment are erased, as

$$\sigma^{n} = 0, \; {}^{n}\epsilon^{el} = 0, \; {}^{n}\epsilon^{\theta} = 0, \; {}^{n}\epsilon^{p} = 0, \; {}^{n}\bar{\epsilon}^{p} = 0 \tag{35}$$

where $\bar{\epsilon}^{p}$ is the equivalent plastic strain in the Mises plasticity.
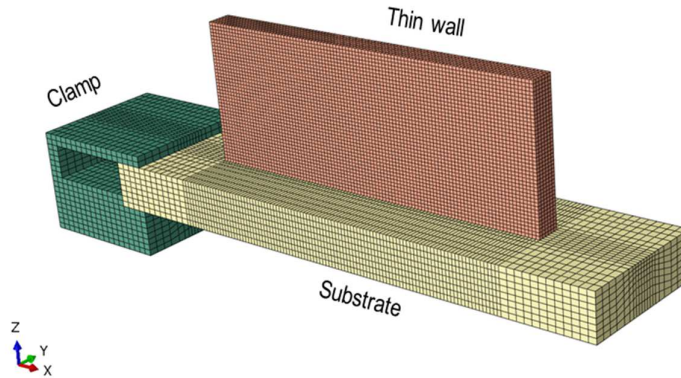
7. Results and Discussions

Figure 5:   FE model of experiments of printing a three-bead wide thin-wall structure

Finite element (FE) simulations of additive manufacturing processes of Ti-6Al-4V parts were carried out using the commercial software Abaqus/Standard using the physics-based framework described above. While material models available in the software could have been used, we have opted to use the more advanced metallurgical phase transformation models described above implemented via user subroutines. A sequential thermal-stress analysis was performed. We modelled the printing process of a thin-wall

structure on a cantilevered substrate using the laser direct energy deposition (LDED) technique, for which experimental results are available (Denlinger *et al.*, 2015b). Figure 5 shows the FE model of the test configuration that consists of a rigid aluminium clamp, a substrate made of solid Ti-6Al-4V, and a thin wall to be built by three-bead depositions per layer and 42-layer depositions in height. A uniform mesh of 1.02 mm $\times$ 1.12 mm $\times 0.907$ mm elements was used for the thin wall.

To model the LDED process, elements of the thin wall along the prescribed laser path in the working layer were progressively activated ahead of the laser beam. The material is activated in the raw state and at ambient temperature prior to being heated by the laser beam. The process parameters are summarized in Table 6.

Power P	2000 W
Absorption Efficiency η	45%
Laser Scan Speed v_x	10.6 mm/s
Laser Spot Radius r	2 mm
Penetration Depth h	1.1 mm
Eccentricity e	1
Time for One-bead Deposition	9.25 s
Cooling Time between Beads	5s
Time for One Layer	42 s
Additional Cooling Time between Layers (Dwell Time)	0 s
Ambient Temperature T_∞	26 °C

Table 6:   Process parameters

Given the formidable time multiscale aspects of the physics involved, a quick study regarding time incrementation was performed. Three time increments were tried to simulate the test: $dt = 0.045$ s, which is the time of laser traversing half of typical element; $dt = 10$ s, which is equivalent to the time of finishing one-bead deposition; $dt = 42$ s, the time of finishing one-layer deposition. Figure 6 shows the snapshots of the computed temperature distributions for the three different time increments as the 14th layer is being printed. A small molten pool can be seen in the case using the element-wise time increment, however, the high temperature transients are not captured when the bead-wise and the layer-wise time increments are used, as expected. The temperature distributions elsewhere are similar for the three cases. The temperature histories at the bottom center of the thin wall are shown in Figure 7, where each data point represents the temperature at that location over time. Rapid heating and cooling cycles are successfully captured using small time increments, and the material exceeds the melting temperature when first deposited. Temperature spikes were missing in the

results when using larger time increments, however the overall temperature profile is still captured well.

Thus, a proper choice of the time increment to balance the accuracy and efficiency of FE simulations of additive manufacturing processes is crucial. The highly concentrated, fast-moving laser heat source leads to local high thermal gradients and rapid temperature changes in workpieces during printing. A smaller time increment can better capture local temperature histories, including all peaks and valleys, which play a determining role when modelling of material-state transitions, solid-phase transformations, and grain structural evolutions. However, using smaller time increments results in higher computational costs, as shown in Table 7. Another interesting finding, counterintuitively, is that using smaller time increments can bring in more difficulties to convergence, due to the use of temperature-dependent thermal properties and the rather discontinuous latent heat effects at material-state transitions. In contrast, a larger time increment is more efficient to obtain overall temperature changes while it will smear the concentrated, fast-moving laser spot out over both space and time, resulting in loss of important local temperature information.
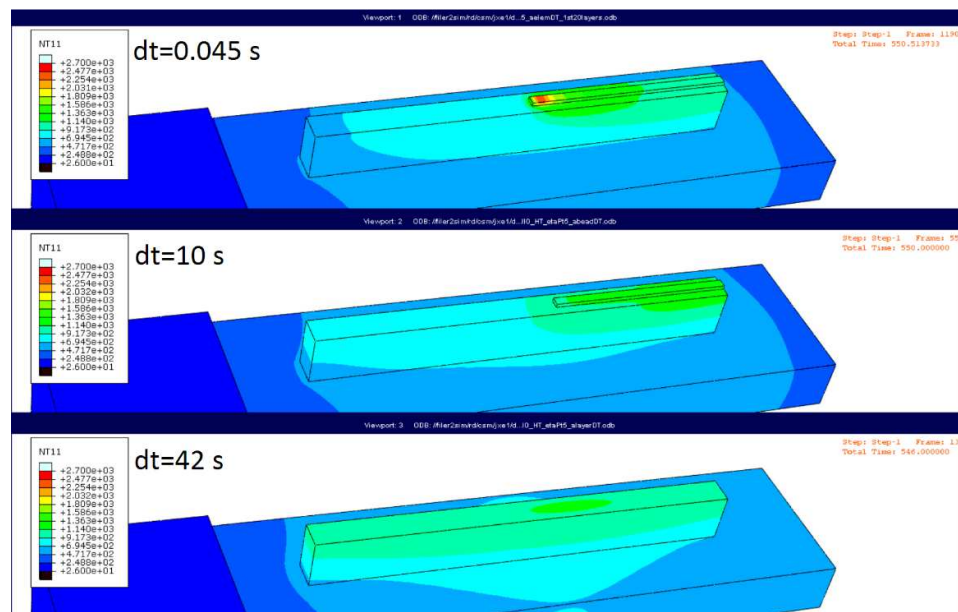

Figure 6:   Simulated temperature distributions when the 14th layer on printing by using different time increments
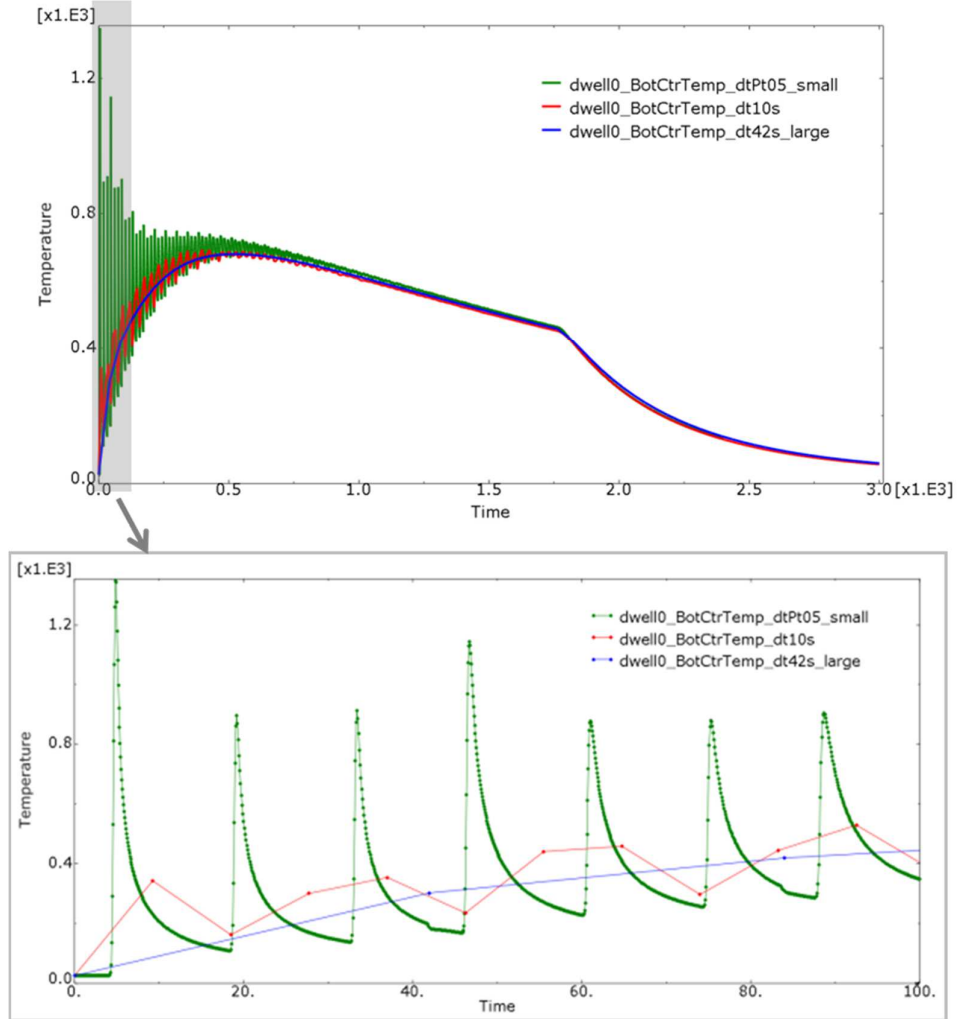
Figure 7:   Simulated temperature histories of the bottom centre of the thin wall by using different time increments

Time Increment	$dt = 0.045$ s	$dt = 10$ s	$dt = 42$ s
Runtime with 16 CPUs	>100 hrs	~50 min	~20 min
Total Number of Increments	66667	300	72
Number of Iterations per Increment	5-9 for heating 1 for cooling	4-6 for heating 1 for cooling	4-6 for heating 1 for cooling

Table 7:   Computational costs of simulations by using different time increments

As shown in Figure 6, temperature at locations far away from the laser path is less sensitive to the choice of time incrementation. Thus, the bead-wise time increment, $dt = 10$ s, was used to validate the calculations of far-field temperature histories and overall distortions. As shown in Figure 8, good agreement can be found between simulations and in-situ experiment measurements of temperature histories of three thermocouples that were placed at the bottom of the substrate. The simulations cool slightly faster than physical tests, but no extensive attempts were made for calibration of the various boundary conditions parameters. Agreement in far-field temperature histories indicates that the energy balance of the system, including heat input by laser, conducting, and cooling by convection and radiation, is well captured. The simplified macroscopic mechanical model with stress relaxation scheme was used to compute the stress response. A comparison of simulated and measured deflection of the free end of the substrate is shown in Figure 9. The final deflection is over-predicted, which is attributed to the faster cooling in the simulation results compared to the physical test, but no attempts were made to recalibrate convection and absorption coefficients or to adopt location dependent convection models.
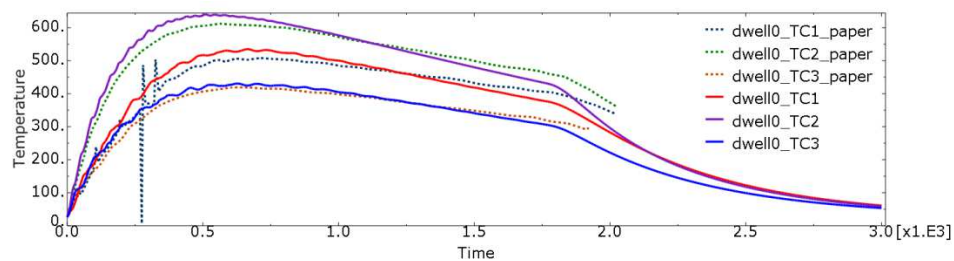

Figure 8:   Comparisons between experimentally measured (dotted lines) and simulated temperature histories of the three thermocouples in the test. Simulations used time increment $dt = 10s$.
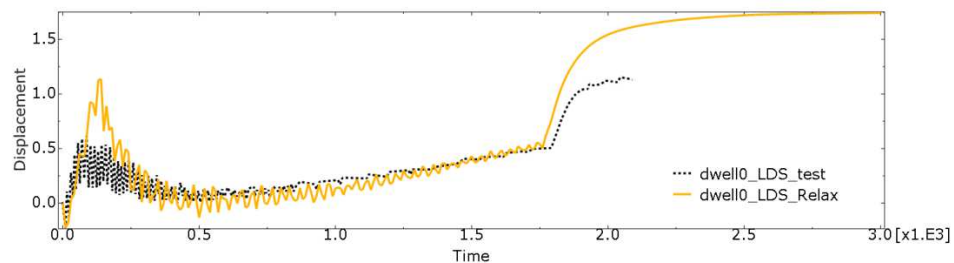

Figure 9:   Comparisons between experiment measured (dotted line) and simulated (solid line) deflection of substrate free end in the test. Simulations used time increment $dt = 10s$.

A small element-wise time increment is required to obtain information of material states, solid-phase composition and transformation activities, grain size, and grain morphology. While the models for microstructure evolution have been fully implemented via user subroutines and tested in some simpler cases, validation against SEM data is in progress and not ready to be shared yet.

8.   Conclusions

Sequential thermo-mechanical modelling of additive manufacturing processes of Ti-6Al-4V parts was presented. Material properties were considered as dependent of temperature and the state of matter. The material state, being raw, liquid or solid, was further determined by local temperature histories. Latent heat effects at material-state transitions were included. A martensitic transformation and two diffusional transformations between three solid-phases (α-, β-, α'-phases) of Ti-6Al-4V were modelled using the Koistinen-Marburger (KM) and Johnson-Mehl-Avrami (JMA) models, respectively. The β grain size was estimated by a semi-empirical growth law. All quantitative descriptions of microstructures, including solid-phase composition and grain size, were updated using an implicit backward Euler method. The β grain morphology, being equiaxed, columnar or their mixture, was estimated by an experimentally calibrated solidification map. Numerically obtained histories of temperature distributions, material states, solid-phase composition and transformation activities, and grain structure further served as input into the mechanical analysis. A macroscopic continuum model proposed for a low-alloy steel has been extended for Ti-6Al-4V. In addition to the classical thermo-elasto-plasticity constitutive relations, transformation induced volume change and plasticity were also considered. Lacking experiment calibrated coefficients of constitutive models, a simplified version using stress relaxation scheme instead from literature was adopted.

The thermal and mechanical models were implemented in Finite Element (FE) simulations using an implicit backward Euler integration scheme. It is important to choose an appropriate time increment in FE analysis to balance the required level of accuracy and computational cost. A smaller time increment can better capture local temperature histories and thermal gradients, as required for modelling of material-state transitions and microstructure evolutions, while a larger time increment is more efficient to obtain overall temperature changes and far-field temperature histories with less convergence problems.

The FE predictions for the far-field temperature histories and distortions of a printed part have been validated with published experiment measurements. The models of microstructure evolutions have been tested in some simple cases, and additional validation is underway. The proposed modelling technique can be helpful in industrial application and process optimization and can also be extended to other metallic materials.

9.   References

Abaqus 2017 User's Manual. https://www.3ds.com/products-services/simulia/support/documentation/

Castro, R., and Seraphin, L. (1966). *Contribution to metallographic and structural study of titanium alloy TA6V:* Memoires Scientifiques de la Revue De Metallurgie, *63.* *1025-1058*

Crespo, A. (2011). *Modelling of heat transfer and phase transformations in the rapid manufacturing of titanium components*. In A. Ahsan, *Convection and Conduction Heat Transfer:* InTech. 315-340.

Crespo, A., Deus, A., and Vilar, R. (2009). *Modeling of phase transformations and internal stresses in laser powder deposition:* XVII International Symposium on Gas Flow, Chemical Lasers, and High-Power Lasers, International Society for Optics and Photonics. 713120-713120

Denlinger, E. R., Heigel, J. C., and Michaleris, P. (2015a). *Residual stress and distortion modeling of electron beam direct manufacturing Ti-6Al-4V:* Proceedings of the Institution of Mechanical Engineers, Part B: Journal of Engineering Manufacture, 229.10. 1803-1813.

Denlinger, E. R., Heigel, J. C., Michaleris, P., and Palmer, T. A. (2015b). *Effect of inter-layer dwell time on distortion and residual stress in additive manufacturing of titanium and nickel alloys:* Journal of Materials Processing Technology, 215. 123–131

Denlinger, E. R., and Michaleris, P. (2016). *Effect of stress relaxation on distortion in additive manufacturing process modeling:* Additive Manufacturing, 12. 51-59.

Fan, Z., and Liou F. (2012). *Numerical modeling of the additive manufacturing (AM) processes of titanium alloy*. In A. K. M. Nurul Amin, *Titanium alloys–towards achieving enhanced properties for diversified applications:* InTech. 3-28.

Gockel, J., and Beuth, J. (2013). *Understanding Ti-6Al-4V Microstructure Control in Additive Manufacturing via Process Maps:* Solid Freeform Fabrication Proceedings, Austin, TX. 12-14.

Goldak, J., Chakravarti, A., and Bibby M. (1984). *A new finite element model for weldingheat sources:* Metall. Trans. B 15 (2). 299–305.

Kobryn, P. A., and Semiatin, S. L. (2003). *Microstructure and texture evolution during solidification processing of Ti-6Al-4V:* Journal of MATERIALS Processing Technology, 135 (2). 330-339.

Mahnken, R., Schneidt, A., and Antretter, T. (2009). *Macro modelling and homogenization for transformation induced plasticity of a low-alloy steel:* Internal Journal of Plasticity, 25(2). 183-204.

Malinov S, Markovsky P, Sha W, and Guo Z (2001). *Resistivity study and computer modelling of the isothermal transformation kinetics of Ti–6Al–4V and Ti–6Al–2Sn–4Zr–2Mo–0.08 Si alloys:* Journal of Alloys and Compounds, 314(1).181-92.

Marion, G., Cailletaud, G., Colin, C., and Mazière M. (2014). *A finite element model for the simulation of direct metal deposition*: ICALEO 2014 Congress Proceedings. Paper 1801.

Mur, F. X. G., Rodriguez, D. and Planell, J. A. (1996). *Influence of tempering temperature and time on the α'-Ti-6Al-4V martensite:* Journal of Alloys and Compounds, 234. 287-289.

Sahoo, S., and Chou, K. (2016). *Phase-field simulation of microstructure evolution of Ti–6Al–4V in electron beam additive manufacturing process*: Additive Manufacturing, 9. 14-24.

Shamsaei, N., Yadollahi, A., Bian, L., and Thompson, S. M. (2015). *An overview of Direct Laser Deposition for additive manufacturing; Part II: Mechanical behavior, process parameter optimization and control:* Additive Manufacturing, 8. 12-35.

Shen, N., and Chou, K. (2012). *Thermal modeling of electron beam additive manufacturing process: Powder sintering effects*: Proceedings of the ASME 2012 International Manufacturing Science and Engineering Conference, Notre Dame, In.

Yin, H., and Felicelli, S.D. (2010). *Dendrite growth simulation during solidification in the LENS process*: Acta Materialia, 58. 1455–1465